# Determining diurnal variations of land surface emissivity from geostationary satellites

Zhenglong Li,[1] Jun Li,[1] Yue Li,[1] Yong Zhang,[2] Timothy J. Schmit,[3] Lihang Zhou,[3] Mitchell D. Goldberg,[3] and W. Paul Menzel[1]

Received 13 June 2012; revised 22 October 2012; accepted 25 October 2012; published 13 December 2012.

[1] Infrared (IR) land surface emissivity (LSE) with a high temporal and spatial resolution is very important for deriving other products using IR radiance measurements as well as assimilating IR radiances in numerical weather prediction (NWP) models over land. Retrieved from various satellite instruments, many LSE databases are available for operational and research use. Most are updated only monthly; assuming emissivity does not change within the month. However, laboratory measurements have shown that emissivity increases by 1.7% to 16% when soil moisture content becomes higher, especially in sandy soils in the 8.2–9.2 $\mu$m range. And a clearly defined wave-like diurnal pattern of decreasing surface soil moisture during the day and recovery (or increased soil moisture) at night was observed. Therefore, it is expected that LSE possesses a diurnal wave-pattern variation with low values during day time and high values during nighttime. The physically based GOES-R ABI LSE algorithm uniquely exploits the geostationary satellites' high temporal resolution. The algorithm was developed and applied to the radiance measurements from the Spinning Enhanced Visible and InfraRed Imager (SEVIRI) on the Meteosat Second Generation (MSG) Meteosat-8/9. The results over the Sahara Desert show that 8.7 $\mu$m emissivity has a significant diurnal wave-pattern variation, with high values during nighttime and low values during day time. 10.8 $\mu$m emissivity also shows a similar diurnal variation, but with a smaller amplitude compared to 8.7 $\mu$m. 12.0 $\mu$m emissivity has an even weaker diurnal variation, and an opposite pattern as 8.7 and 10.8 $\mu$m. Evidence is provided to demonstrate that the SEVIRI LSE diurnal wave-pattern variations are real, not artifacts from the retrieval algorithm. The impacts of diurnal variations of errors in GFS forecast (temperature and moisture profiles) and in land surface temperature (LST) are analyzed; they are found to be minor compared to the LSE diurnal variations shown by SEVIRI.

**Citation:** Li, Z., J. Li, Y. Li, Y. Zhang, T. J. Schmit, L. Zhou, M. D. Goldberg, and W. P. Menzel (2012), Determining diurnal variations of land surface emissivity from geostationary satellites, *J. Geophys. Res.*, *117*, D23302, doi:10.1029/2012JD018279.

## 1. Introduction

[2] Land surface emissivity (LSE) is the relative ability of the land surface to emit energy by radiation. It is defined as the ratio of the energy radiated by the land surface to energy radiated by a blackbody at the same temperature. Infrared (IR) LSE varies with land surface type (according to soil type, land cover, and land use [*Snyder et al.*, 1998; *Peres and DaCamara*, 2005], viewing angle [*Francois et al.*, 1997; *McAtee et al.*, 2003], and time, following changes in the state of soil moisture, vegetation, and weather conditions, such as dew/frost formation, evaporation, rainfall, or snowfall).

[3] Accurate IR LSE with a high temporal resolution and a high spatial resolution plays an important role in land surface modeling, weather forecasting, as well as deriving other satellite products. *Jin and Liang* [2006] reported that inaccurate LSE induces warm bias as large as 1.5 K for surface air temperature in modeling the land surface energy budget. Progress has been made in assimilating satellite IR radiances to improve weather forecasting skills [*Le Marshall et al.*, 2006; *English et al.*, 2000; *McNally et al.*, 2006]. However, due to lack of accurate IR LSE, it remains challenging to assimilate satellite radiances in thermal IR region (8–12 $\mu$m) [*McNally et al.*, 2006], which contain information about surface and lower atmosphere. Accurate IR LSE is also needed for temperature and moisture retrievals from the Geostationary Operational Environmental Satellite (GOES) Sounder and other IR sounders [*Menzel and Purdom*, 1994;

[1]Cooperative Institute for Meteorological Satellite Studies, University of Wisconsin-Madison, Madison, Wisconsin, USA.
[2]National Meteorological Satellite Center, China Meteorological Administration, Beijing, China.
[3]Center for Satellite Applications and Research, NESDIS, NOAA, Madison, Wisconsin, USA.

Corresponding author: Z. Li, 1225 West Dayton St., Madison, WI 53706, USA. (zhenglong.li@ssec.wisc.edu)


0148-0227/12/2012JD018279

*Menzel et al.*, 1998; *Ma et al.*, 1999; *Li and Huang*, 1999; *Li et al.*, 2000; *Jin et al.*, 2008; *Li et al.*, 2008, 2009; *Liu et al.*, 2008]. *Seemann et al.* [2008] demonstrated that accurate LSE could improve the root mean squared error (RMSE) of the retrieved Moderate Resolution Imaging Spectroradiometer (MODIS) total precipitable water (TPW) from 3.8 mm to 2.5 mm. Inaccurate IR LSE is one important error source of the satellite derived land surface temperature [*Becker and Li*, 1990; *Wan and Dozier*, 1996; *Yu et al.*, 2008]. Other satellite products that require accurate IR LSE include but not limited to radiation budget [*Lee et al.*, 2007], trace gas retrievals [*Clerbaux et al.*, 2003; *Ho et al.*, 2005], dust and aerosol property retrievals [*Zhang et al.*, 2006; *Li et al.*, 2007a], and the cloud top pressure (CTP) product [*Menzel et al.*, 1992, 2008; *Li et al.*, 2001, 2005].

[4] Temporal variations of IR LSE, specially the diurnal variations, are poorly studied. According to *Mira et al.* [2007], the laboratory measurements show that emissivity increases by 1.7% to 16% when soil moisture content becomes higher, especially in sandy soils in the 8.2–9.2 $\mu$m range. This emissivity increasing with increased soil moisture is also reported by other studies using either laboratory experiments or satellite remote sensing techniques [*Ogawa et al.*, 2006; *Hulley et al.*, 2010; *Sanchez et al.*, 2011]. *Jackson et al.* [1997] reported 1) the soil moisture diurnal variations as a clearly defined diurnal pattern (wave) of decreasing surface moisture during the day and recovery (or increased soil moisture) at night; and 2) water loss at the near surface beginning 1 to 2 h before sunrise and a re-moistening beginning 2 to 4 h before sunset. Based on these observations, it is expected that the LSE have diurnal variation where there are diurnal variations of soil moisture at the near surface; LSE, especially in 8.2–9.2 $\mu$m range in desert area, are expected to have high values at nighttime and low values during day time. Many NWP and climate models still use static maps with a limited number of possible emissivity values prescribed per surface type [*Jin and Liang*, 2006; *Ogawa and Schmugge*, 2004; *Trigo and Viterbo*, 2003].

[5] IR LSE can be derived from satellite radiance measurements on either Geostationary Orbit (GEO) or the polar orbiting low earth orbit (LEO). Most of the LSE databases are LEO products because of the global coverage. However, since LEO satellites only observe a same location twice a day, those LSE databases are not able to fully capture LSE diurnal variations. For example, a monthly global database [*Seemann et al.*, 2008] has been developed based on the MODIS emissivity product [*Wan and Li*, 1997; *Wan*, 2008] and hyperspectral IR emissivity measurements from laboratory measurements. Hyperspectral resolution IR sounders onboard LEO satellites, such as the Atmospheric Infrared Sounder (AIRS) [*Chahine et al.*, 2006] onboard the NASA Earth Observing System (EOS) Aqua platform, the Interferometer Atmospheric Sounding Instrument (IASI) onboard the European Meteorological Operational Satellite Programme (METOP-A) [*Hilton et al.*, 2012], and the Cross-track Infrared Sounder (CrIS) on the U.S. Suomi National Polar-orbiting Partnership (NPP) and later the Joint Polar-orbiting Satellite System (JPSS), are capable of retrieving the emissivity spectrum. Algorithms have been developed for retrieving hyperspectral IR emissivity spectra from global advanced IR sounder radiance measurements [*Li et al.*, 2007b; *Zhou et al.*, 2008; *Li and Li*, 2008].

[6] In this study, the U.S. next generation of Geostationary Operational Environmental Satellite (GOES-R series) Advanced Baseline Imager (ABI) LSE algorithm [*Schmit et al.* 2005; *Li et al.*, 2011] is applied to SEVIRI [*Schmetz et al.*, 2002] radiance measurements. The retrieved SEVIRI LSE show strong diurnal variations, especially for the 8.7 $\mu$m band. Evidence is provided to show that the LSE diurnal variations are real, not artifacts from the retrieval algorithm. This study is part of GOES-R ABI LSE algorithm [*Li et al.*, 2011] validation. However, instead of validation using real LSE measurements, which are difficult to obtain, this study focuses on demonstrating LSE diurnal variations using satellite radiance measurements.

## 2. SEVIRI LSE Case Demonstration

[7] The GOES-R ABI LSE algorithm [*Li et al.*, 2011] is applied to SEVIRI radiance observations. The algorithm is based on the unique concept from geostationary satellites, the so-called time continuity, which assumes LSE does not change during a short period of time while the land surface temperature (LST) does. In the algorithm, three time steps are used to strengthen the LSE signals, which are usually difficult to separate from the LST signals. The time interval between two consecutive time steps is three hours, which is based on the following considerations, (1) the LSE does not change during a short time period, and (2) the land surface temperature has a relatively large temporal variation during that time period. The monthly baseline fit LSE database [*Seemann et al.*, 2008] is used as first guess. Despite the fact that the retrieved LSE is an average of three time steps (a time span of 6 h), the algorithm is still able to capture the LSE diurnal variation in the Sahara Desert. For more details about the GOES-R ABI LSE algorithm, refer to *Li et al.* [2011].

[8] Figure 1 shows 8.7 $\mu$m LSE imagery, from August 2006, for the first guess and the SEVIRI retrievals over the Sahara Desert (20°N–35°N, 20°W–40°E). This region is specially chosen because LSE in sandy soil is expected to be more sensitive to soil moisture [*Mira et al.*, 2007]. The top panel is from the baseline fit database used as first guess for the SEVIRI retrieval algorithm, and the middle and the lower panels are the SEVIRI retrievals, from 02 UTC and 14 UTC, respectively. These two times represent the nighttime (maximum LSE) and day time (minimum LSE) of LSE during a 24-h cycle, as will be shown in Figure 5. The LSE at each pixel is an average of all available retrievals at that pixel for that specific hour during August 2006.

[9] Comparing the SEVIRI retrievals with the baseline fit database, the geographic distribution is highly similar, indicating that both the GOES-R ABI LSE algorithm and the baseline fit database are effective on discriminating deserts from other surface types. However, there are noticeable differences. The low value area (blue) of SEVIRI LSE has slightly higher values than the baseline fit database; and the high value area (red) has slightly lower values than the baseline fit database. This indicates that the SEVIRI LSE algorithm makes substantial changes over the first guess. No attempt is made in this study to address whether the baseline fit or the SEVIRI LSE is closer to the truth. Rather, the

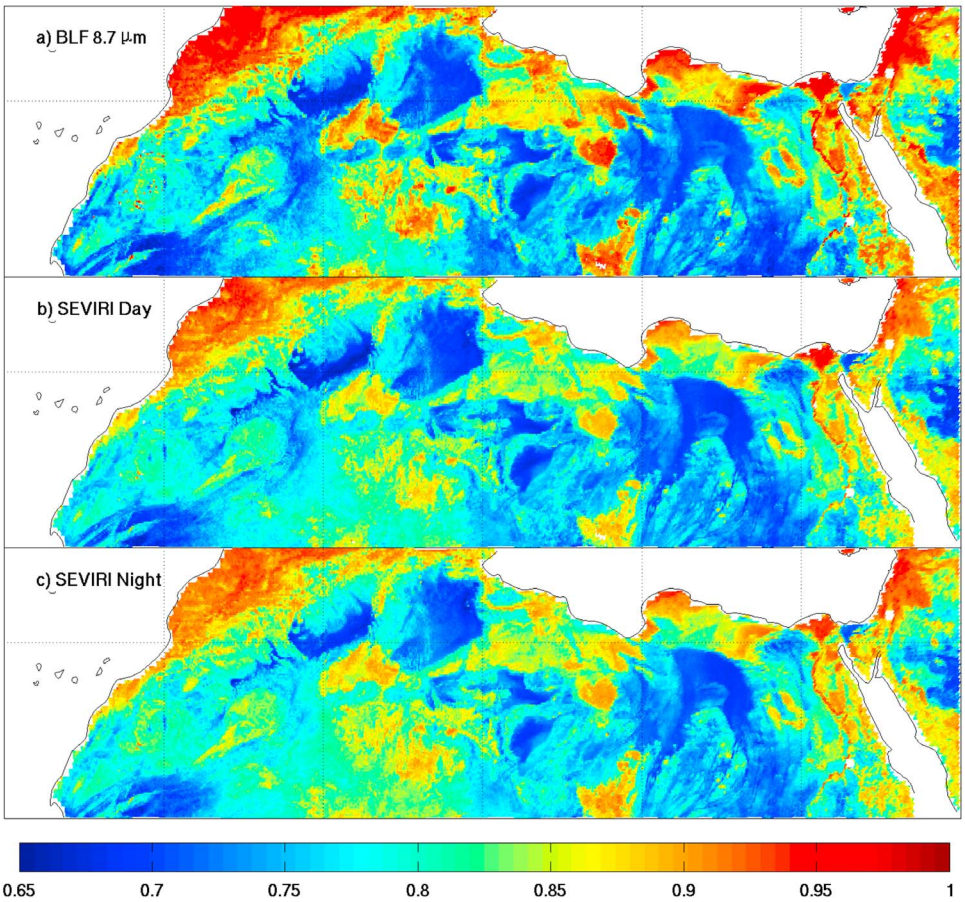


**Figure 1.** 8.7 $\mu$m LSE one-month composite of August 2006 from (a) the baseline fit database, (b) the day time SEVIRI at 14 UTC and (c) the nighttime SEVIRI at 2 UTC.

SEVIRI LSE will be used to demonstrate the LSE diurnal variations, whereas the baseline fit database is incapable of. There are considerable differences between the day time and nighttime SEVIRI LSE. In areas of low LSE, the day time LSE is smaller than the nighttime.

[10] Figures 2 and 3 show same imagery as Figure 1 except for 10.8 and 12 $\mu$m. Similarity is observed between the baseline fit database and the SEVIRI LSE. And there exist substantial differences of the SEVIRI LSE between the day time and the nighttime, with day time values being lower and nighttime values being higher for both 8.7 and 10.8 $\mu$m. The 12 $\mu$m shows the opposite, with day time being higher values and nighttime being lower values. Visually, the day/night difference of 8.7 $\mu$m is less profound than 10.8 and 12 $\mu$m because of a larger color bar range. But 8.7 $\mu$m actually sees more day/night differences than 10.8 $\mu$m.

[11] Figure 4 shows the differences between the day time and the nighttime (the former minus the later). Note that the color bar is different for the three channels. The west half of Sahara Desert shows much more (in absolute value) day/night differences than the east half. The 8.7 $\mu$m shows the largest day/night differences among the three channels. Some regions (dark blue) have day/night differences more than 0.03 (day time LSE is 0.03 smaller than nighttime LSE). Since the temporal average is performed to generate these one-month composite imagery, the day/night differences during a specific day could be much larger than 0.03 in absolute value. The 10.8 $\mu$m shows smaller day/night differences compared with 8.7 $\mu$m. There are regional differences close to $-0.02$. Both 8.7 and 10.8 $\mu$m show that the day time LSE is smaller than nighttime in most of the regions. This is consistent with the expectation stated in the introduction section. These diurnal variations are likely results of soil moisture content changes. The 12 $\mu$m also shows diurnal variations in the same region, but with even smaller differences and an opposite phase.

[12] Figure 4 clearly shows that there are differences of the retrieved SEVIRI LSE between the day time and nighttime. This indicates that there might exist LSE diurnal variations (wave-like). To better discern any LSE diurnal variations, the following procedure was used. For each day, a 24-h cycle from 0000 UTC to 2359 UTC is processed hourly; if a pixel has retrievals for all the 24 nominal hours, it is retained. For each of the 24 h, an area average is performed to calculate the LSE diurnal variation for that day. The daily LSE diurnal variations are then averaged to generate one single diurnal variation for a period of time. Figure 5 shows the LSE diurnal variation for the three SEVIRI window channels for August 2006, along with three other time periods.

[13] For 8.7 $\mu$m, a clearly defined wave-like diurnal pattern is observed for all the four time periods, with maximum values at night and minimum values in the day, consistent

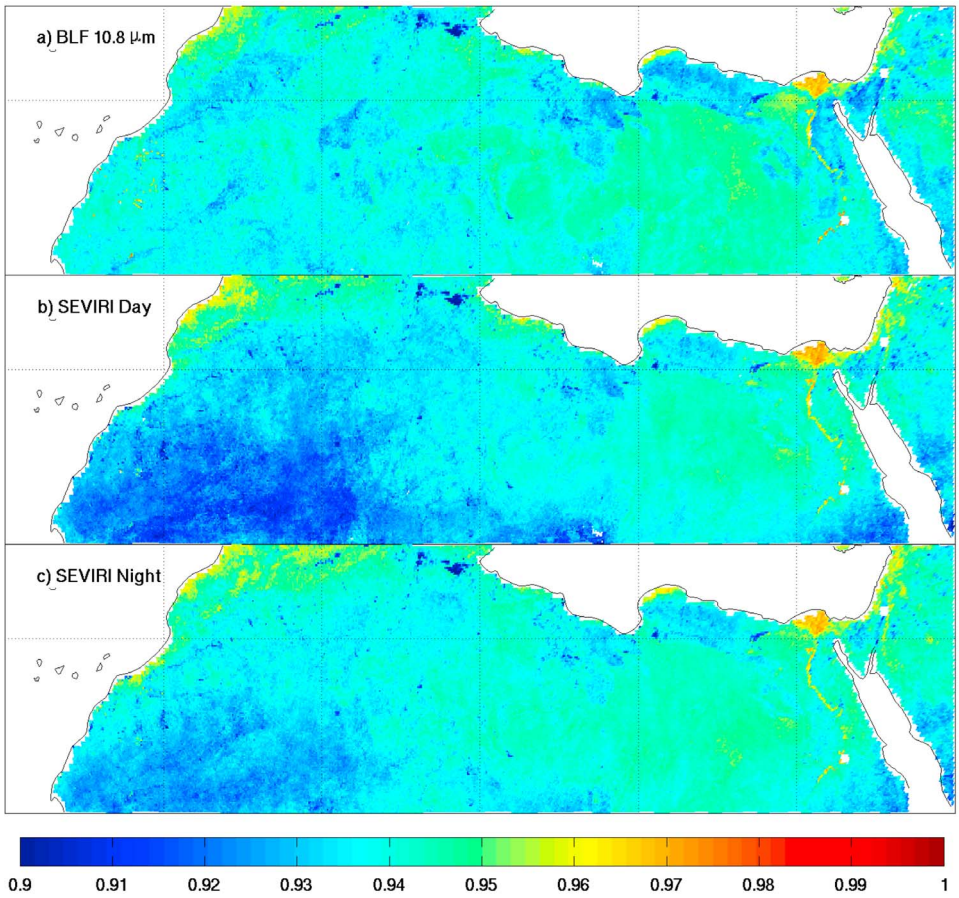


**Figure 2.** 10.8 $\mu$m LSE one-month composite of August 2006 from (a) the baseline fit database, (b) the day time SEVIRI at 14 UTC and (c) the nighttime SEVIRI at 02 UTC.

with the discussion in the introduction section. The diurnal variation strength (DVS) is defined as the local minimum or maximum during the day minus the local maximum or minimum at night. A negative value indicates day time LSE is smaller than nighttime LSE; and a positive value indicates day time LSE is larger than nighttime LSE. The values are listed in Table 1. The LSE during April 2007 shows the strongest diurnal variation, with a DVS of $-0.0225$, while the October 2007 LSE shows the weakest diurnal variation, with a DVS of $-0.0040$. Three of the four time periods show that 10.8 $\mu$m has a similar wave-like but weaker diurnal pattern than 8.7 $\mu$m, with the exception of October 2007, which has an opposite phase with a very small DVS of 0.0011. The DVS of 10.8 $\mu$m is roughly 1/3 of that of 8.7 $\mu$m in absolute value. No attempt is made to investigate if the diurnal variation shown for October 2007 is true or not. However, because the diurnal variation is so small, it is a good approximation to assume LSE has no diurnal variation during that time. The 12 $\mu$m also shows diurnal variations. Except for the October 2007 case, the other three cases show opposite diurnal variation pattern as 8.7 $\mu$m, with DVSs about 1/6 of 8.7 $\mu$m in absolute value. No attempt is made to investigate if the diurnal variation shown for 12 $\mu$m is real or not. However, as will be shown in section 4, the diurnal variations of the three IR window channels are consistent with the analysis of SEVIRI and MODIS/Aqua radiances, indicating that the LSE diurnal variations demonstrated are reasonable. Since this study focuses on LSE diurnal variations, no attempt is made to explain the LSE seasonal variations shown in Figure 5.

[14] Results in Figure 5 are area and time averaged. Individual pixels might possess larger or smaller diurnal variations, depending on the surface and atmospheric conditions. If the diurnal variations shown in Figure 5 are true, omission of diurnal variations will result in bias when deriving other products or assimilating window channel IR radiances over land. The question is whether the diurnal variations shown in Figure 5 are real. In the following sections, satellite radiance observations from SEVIRI are used to support that the LSE diurnal variations are from the satellite observations, not artifacts from the retrieval algorithm. The MODIS/Aqua radiance observations are used as an independent verification.

[15] It is worth to point out that the dew formation is not the major reason for the cases demonstrated above. Dew forms only if the LST is colder than the dew point (Td) near the surface. Figures 6a–6d shows the coldest mean temperature difference during a 24-h cycle between the SEVIRI LST (retrieved simultaneously with the LSE) and the GFS surface Td (the former minus the latter) for the four time periods. The procedures to plot these figures are: 1) for each pixel at x UTC, all available data are averaged to generate the mean LST-Td for x UTC; 2) for each pixel, the minimum

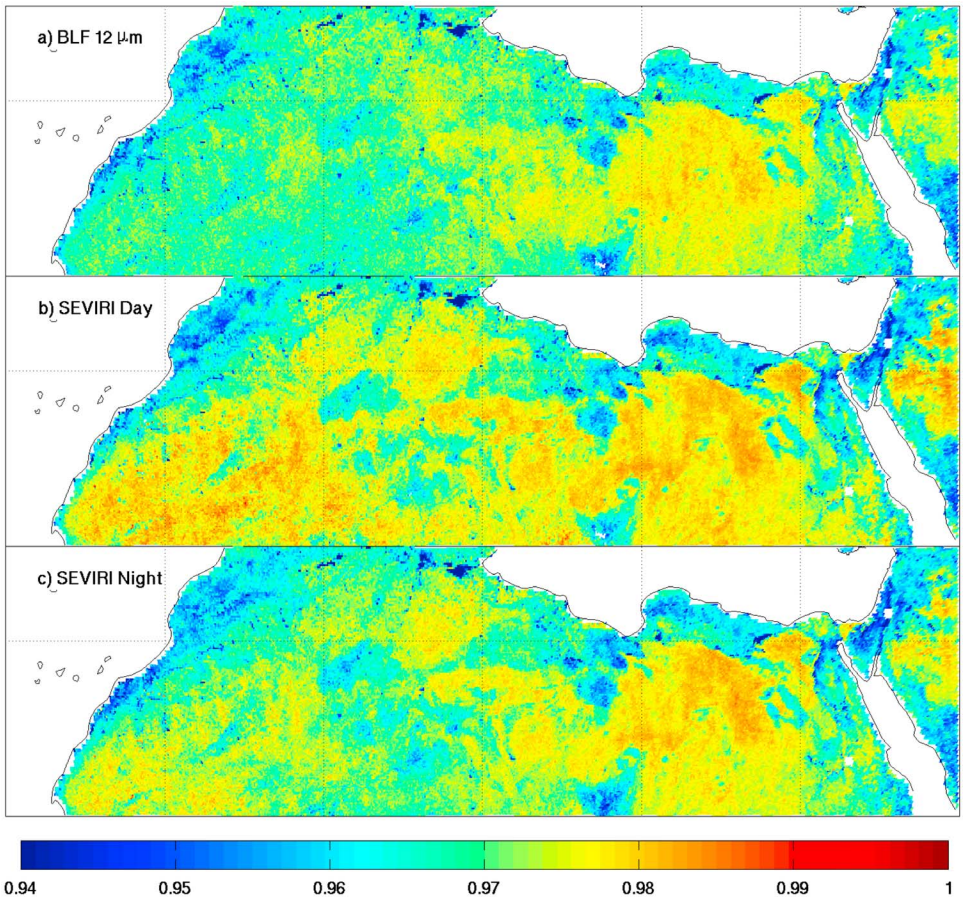


**Figure 3.** 12 $\mu$m LSE one-month composite of August 2006 from (a) the baseline fit database, (b) the day time SEVIRI at 14 UTC and (c) the nighttime SEVIRI at 2 UTC.

among the 24-h cycle is chosen to represent the coldest mean difference between SEVIRI LST and the GFS Td. Figure 6e shows the normalized histograms of Figures 6a–6d. From these figures, it is clear that dew is unlikely to form in most of the area in Sahara Desert. Some dew might form in the coastal area where there is more moisture in the air than in the inner Saharan Desert. According to *Agam and Berliner* [2004, 2006], even the LST is colder than the Td, it is possible that no dew forms in desert. While it is still unknown how dominant the water vapor adsorption (physical adsorption of water vapor from air to soil) is over dew formation, it is clear that in desert area and in very dry conditions, the water vapor adsorption could be dominant [*Agam and Berliner*, 2006]. In other words, the dew formation could occur rarely. This explains the soil moisture content diurnal variation in the desert area without precipitation and dew/frost. This is consistent with the previous studies [*Kidron*, 2000; *Agam and Berliner*, 2006], which suggest that the dew formation is more difficult on bare soil (such as bare sand in Saharan Desert) than vegetation cover and artificial surfaces.

## 3. Method for Detecting LSE Diurnal Variations From Satellite

[16] The top of atmosphere (TOA) clear sky IR window spectral brightness temperature (Tb) may be observed by satellites ($R^o$), or calculated using a radiative transfer equation (RTE), if neglecting scattering by the atmosphere

$$R^c = \varepsilon B(T_s)\tau_s - \int_0^{p_s} B(T)d\tau(0,p) + (1-\varepsilon)\int_0^{p_s} B(T)d\tau^* + R' + e, \quad (1)$$

where $R^c$ is the calculated exiting radiance at TOA, $\varepsilon$ is the surface emissivity, $B(T)$ is the Planck function of temperature T, subscript $s$ denotes the surface, $\tau(0,p)$ is the atmospheric transmittance from the top to the atmospheric pressure $p$, $\tau^* = \tau_s^2/\tau$ is the downwelling transmittance, $e$ is forward model uncertainty and $R'$ is the reflected solar radiation, which is ignored in the longwave IR window region. As shown in equation (1), the TOA IR radiance has three major contributions: the surface emission, the upwelling atmosphere emission, and the reflection of the downwelling atmosphere emission by the surface.

[17] In this section, $\sigma$ is error, $\delta$ is channel difference and $\Delta$ is temporal variation. And diurnal variation is defined as day time minus nighttime. Assuming that the input parameters for the RTE are close enough to the true state of the atmosphere and the surface, the difference between the satellite-observed and calculated Tb is

$$R^c - R^\circ = K_{T_s}\sigma_{T_s} + K_\varepsilon\sigma_\varepsilon + \sum K_T\sigma_T + \sum K_{\ln Q}\sigma_{\ln Q} + e', \quad (2)$$

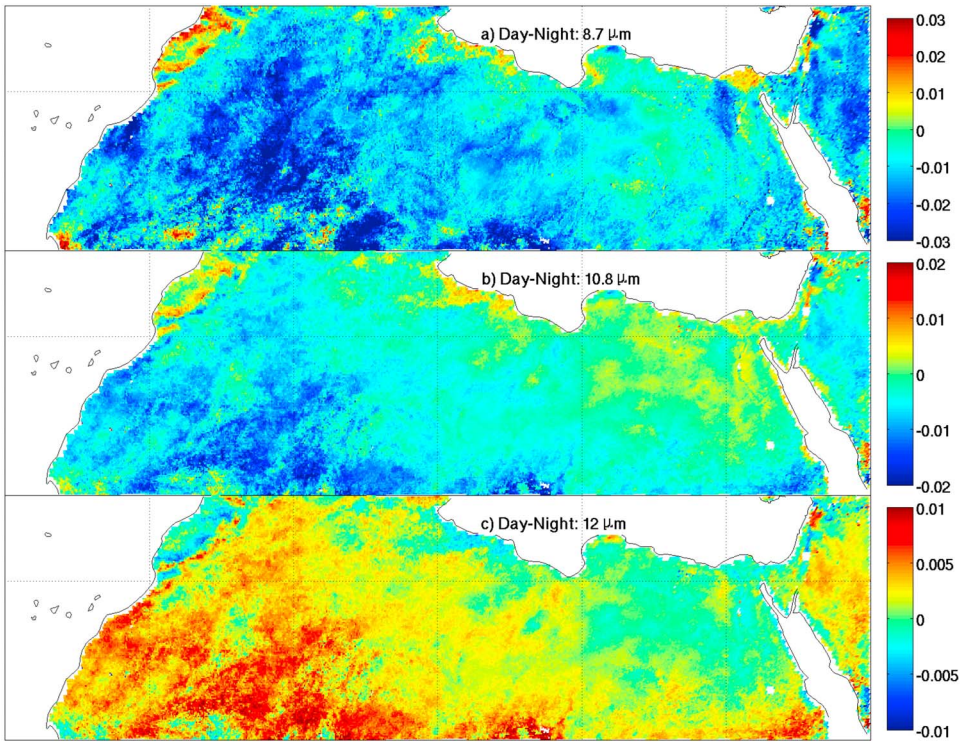


**Figure 4.** Day/night differences of SEVIRI LSE in August 2006 for (a) 8.7, (b) 10.8 and (c) 12 $\mu$m.

where $K_{T_s}$, $K_\varepsilon$, $K_T$ and $K_{\ln Q}$ are kernel functions for LST, LSE, atmospheric temperature and atmospheric mixing ratio, respectively. The kernel function is defined as $K_x = \frac{\partial R}{\partial x}$, where $x$ is the variable used for radiative transfer calculations. It shows the sensitivity of the Tb at TOA with respect to the change in the variable x. The kernel functions are calculated using the analytical approximation method [*Li*, 1994] to reduce computation. $\sigma_{T_s}$, $\sigma_\varepsilon$, $\sigma_T$, and $\sigma_{\ln Q}$ are the error of LST, LSE, atmospheric temperature and atmospheric mixing ratio, respectively. Specifically, for LSE, $\sigma_\varepsilon = \varepsilon - \varepsilon_T$, where $\varepsilon$ is the LSE used for the radiative transfer calculation and $\varepsilon_T$ is the true LSE. $\Sigma$ is the sum over different atmospheric layers used by the RTE. $Q$ is the water vapor mixing ratio. Notice the logarithm of the mixing ratio is used because it has a better linear relationship with Tb. $e'$ in equation (2) contains both forward model uncertainty and observation noise. Equation (2) shows that the Tb difference has three components: the LST, the LSE, and the atmosphere (including the temperature and the moisture profiles). Any departure of these parameters from the true state results in departure of the calculated Tb from the observed ones.

[18] Equation (2) is difficult to evaluate LSE diurnal variation because 1) all of the four variables on the right hand side might have diurnal variations, and make substantial contributions; 2) the radiative transfer model might not be accurate enough and introduce some false diurnal variation due to the difficulty in simulating moisture absorption and local zenith angle dependency. For any two channels $i$ and $j$, the difference between them, or the double difference of Tb

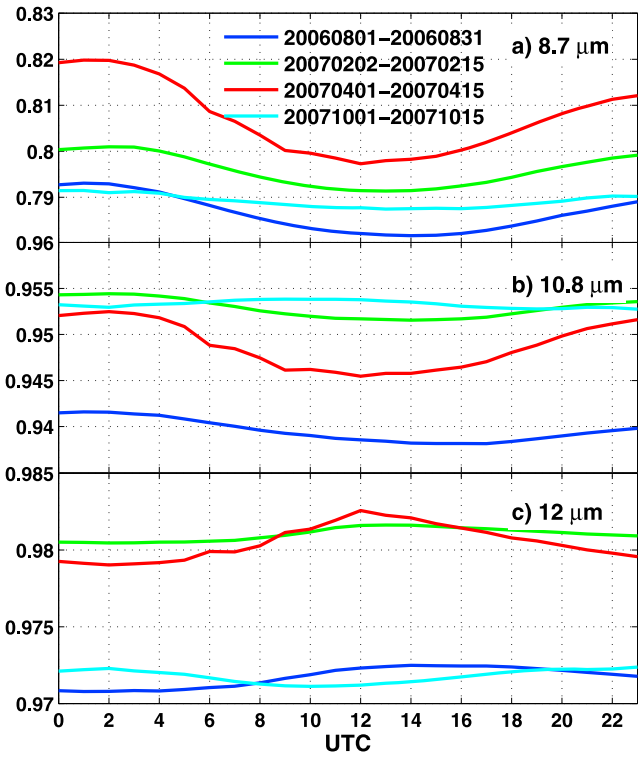


**Figure 5.** (a–c) The averaged hourly SEVIRI LSE diurnal variations over the Sahara Desert during different time periods.

**Table 1.** The LSE Diurnal Variation Strength (Local Minimum/Maximum During the Day Time Minus Local Maximum/Minimum at Night) of the Three SEVIRI Window Channels During Different Times

| Time | 8.7 $\mu$m | 10.8 $\mu$m | 12 $\mu$m |
|---|---|---|---|
| 20060801–20060831 | −0.0114 | −0.0034 | 0.0017 |
| 20070202–20070215 | −0.0096 | −0.0029 | 0.0012 |
| 20070401–20070415 | −0.0225 | −0.0070 | 0.0035 |
| 20071001–20071015 | −0.0040 | 0.0011 | −0.0013 |

(*DDTb*) is defined as $DDTb = R_i^c - R_i^o - \left(R_j^c - R_j^o\right)$. It can be written as

$$DDTb = \delta K_{T_s}\sigma_{T_s} + K_\varepsilon^i\sigma_\varepsilon^i - K_\varepsilon^j\sigma_\varepsilon^j + \sum \delta K_T\sigma_T + \sum \delta K_Q\sigma_{\ln Q}, \quad (3)$$

where $\delta K_{T_s}$, $\delta K_T$, and $\delta K_Q$ are the kernel function differences of LST, temperature profile and the moisture profile between channel $i$ and $j$. Superscript $i$ and $j$ denote channel indices. Equation (3) is different from equation (2) in that the atmospheric contribution terms (the last two terms) can be omitted [*Li et al.*, 2010] for window channels having similar atmospheric transmittance profile. Detailed discussion on the impacts of neglecting the atmospheric terms is presented in section 5. Neglecting the atmospheric terms, equation (3) can be written as

$$DDTb = \delta K_{T_s}\sigma_{T_s} + \delta\bar{K}_\varepsilon^{i,j}\left(\sigma_\varepsilon^i - \sigma_\varepsilon^j\right), \quad (4)$$

where $\delta\bar{K}_\varepsilon^{i,j} = \dfrac{K_\varepsilon^i\sigma_\varepsilon^i - K_\varepsilon^j\sigma_\varepsilon^j}{\sigma_\varepsilon^i - \sigma_\varepsilon^j}$ is the weighted mean LSE kernel function of channels $i$ and $j$, and $\sigma_\varepsilon^i - \sigma_\varepsilon^j$ is the channel difference of LSE error.

[19] For any two times, the temporal variation of *DDTb* is

$$\Delta DDTb = \delta\hat{K}_{T_s}\Delta\sigma_{T_s} + \delta\hat{\bar{K}}_\varepsilon^{i,j}\Delta\left(\sigma_\varepsilon^i - \sigma_\varepsilon^j\right), \quad (5)$$

where $\Delta DDTb$ is the temporal variation of *DDTb*, $\delta\hat{K}_{T_s}$ is the temporal mean of LST kernel function difference of channels $i$ and $j$, $\Delta\sigma_{T_s}$ is the temporal variation of LST error,

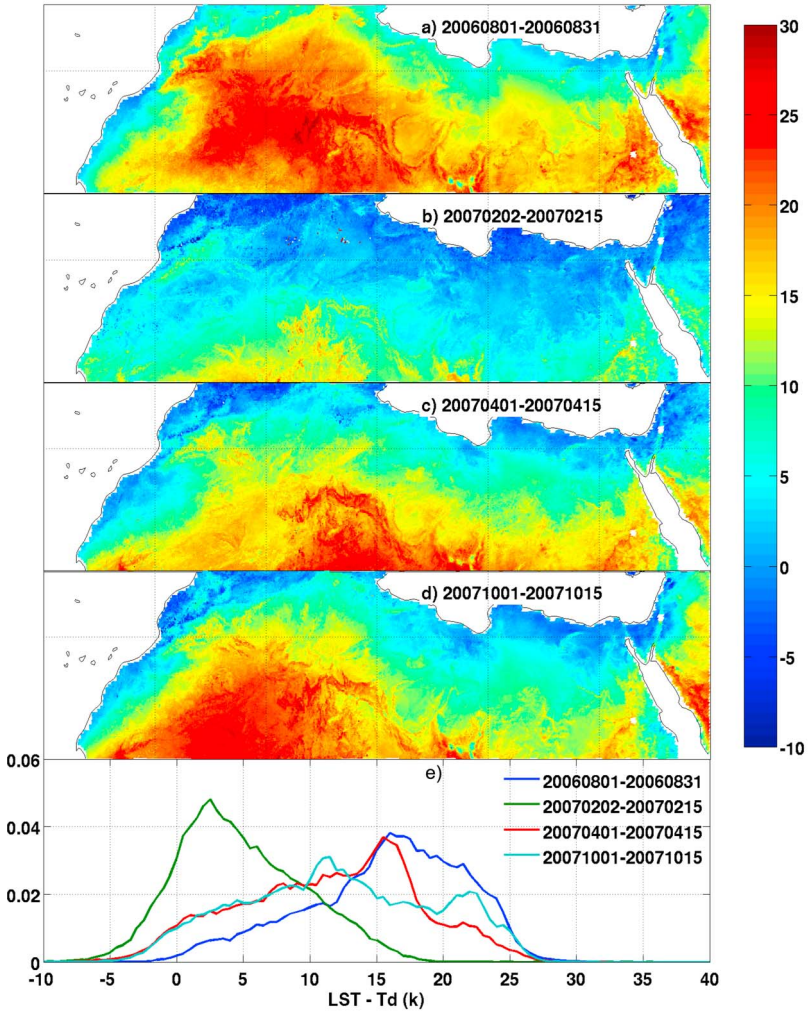


**Figure 6.** The coldest mean temperature difference between LST and Td (former minus latter) from (a) Aug 2006, (b) Feb 2007, (c) Apr 2007, and (d) Oct 2007. (e) The normalized histograms of Figures 6a–6d.

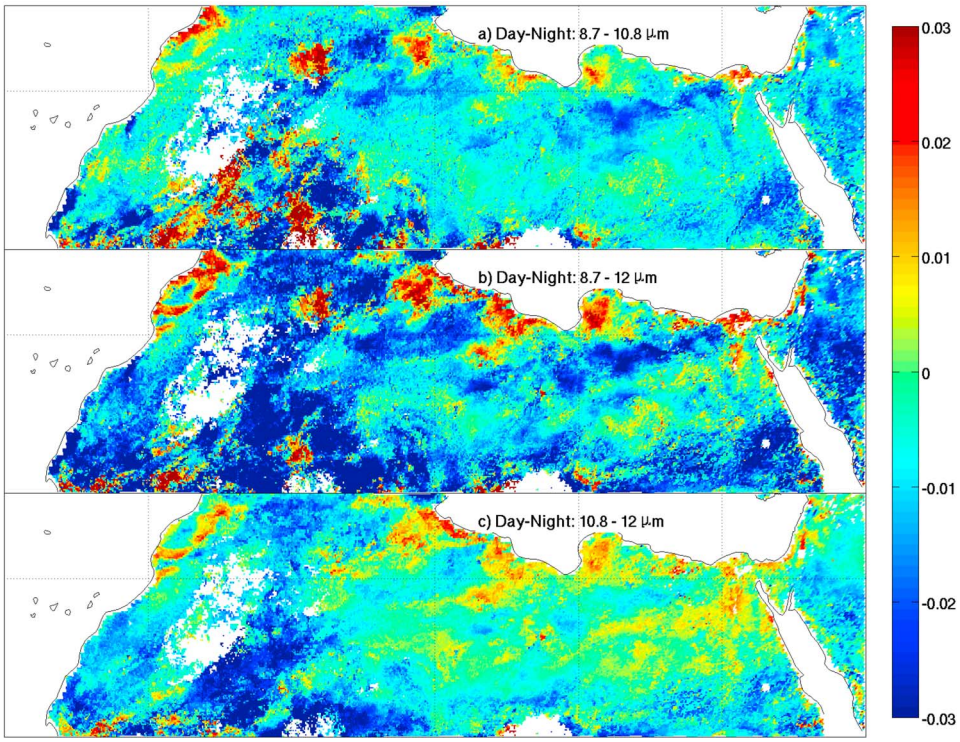


**Figure 7.** Day/night differences of SEVIRI LSE channel difference for August 2–7 2006 for (a) 8.7–10.8 $\mu$m, (b) 8.7–12 $\mu$m and (c) 10.8–12 $\mu$m.

$\delta\hat{\bar{K}}_{\varepsilon}^{i,j}$ is the temporal mean of the weighted mean LSE kernel function of channels $i$ and $j$,, and $\Delta\left(\sigma_{\varepsilon}^{i}-\sigma_{\varepsilon}^{j}\right)$ is the temporal variation of $\sigma_{\varepsilon}^{i}-\sigma_{\varepsilon}^{j}$. Both the LST and LSE kernel functions have temporal variations. So do the $\delta K_{T_s}$ and $\delta\bar{K}_{\varepsilon}^{i,j}$. Sensitivity studies (not shown) have indicated that the use of $\delta\hat{K}_{T_s}$ and $\delta\hat{\bar{K}}_{\varepsilon}^{i,j}$ does not introduce any significant amount of error; the impacts on the LSE diurnal variation analysis can be neglected. Since a static LSE is used for radiative transfer calculation, it can be shown that $\Delta\sigma_{\varepsilon}^{i}=-\Delta\varepsilon_{T}^{i}$, where $\Delta\varepsilon_{T}^{i}$ is the true LSE temporal variation, and $\Delta\left(\sigma_{\varepsilon}^{i}-\sigma_{\varepsilon}^{j}\right)=-\Delta\left(\varepsilon_{T}^{i}-\varepsilon_{T}^{j}\right)$, where $\varepsilon_{T}^{i}-\varepsilon_{T}^{j}$ is channel difference of true LSE temporal variation. Equation (5) can be written as

$$-\Delta DDTb=-\delta\hat{K}_{T_s}\Delta\sigma_{T_s}+\delta\hat{\bar{K}}_{\varepsilon}^{i,j}\Delta\left(\varepsilon_{T}^{i}-\varepsilon_{T}^{j}\right), \qquad (6)$$

Equation (6) shows that the negative of temporal variation of *DDTb*, has a linear relationship with the temporal variation of LST error, and the channel difference of true LSE temporal variation. It is the basis of using satellite radiance observations to demonstrate LSE diurnal variations. It will be used in two different ways. Qualitatively, if LSE diurnal variation dominates on the right hand side of equation (6), $-\Delta DDTb$ should have a similar diurnal variation pattern as LSE channel difference, which will be shown by SEVIRI radiance observations in section 4.1. Quantitatively, equation (6) can be used to estimate diurnal variation of $-\sigma_{T_s}$ and the mean LSE kernel functions. Using different satellite observations should yield a similar estimate of the mean LSE kernel function. This will be shown in section 4.2.

## 4. LSE Diurnal Variations Using Satellite Radiance Observations

[20] Figures 1–5 show significant LSE diurnal variations of 8.7 $\mu$m, substantial LSE diurnal variations of 10.8 $\mu$m, and weak LSE diurnal variations of 12 $\mu$m from SEVIRI. In this section, evidence will be provided to demonstrate that the LSE diurnal variations are real, not artifacts from the retrieval algorithm, using the method introduced in section 3. There are four different time periods shown in Figure 5. Without loss of generality, August of 2006 is chosen for demonstration; note August 2006 shows weaker diurnal variations than April 2007. To further reduce the computation, only 6 days, Aug 2–7 of 2006 are demonstrated.

### 4.1. Evidence From SEVIRI Radiance Observations

[21] In order to use equation (6), clear sky calculated SEVIRI radiances are needed, which are calculated using the Pressure-Layer Fast Algorithm for Atmospheric Transmittance (PFAAST) models [*Hannon et al.*, 1996]. PFAAST is based on the line-by-line radiative transfer model (LBLRTM) version 8.4 [*Clough and Iacono*, 1995] and the high-resolution transmission molecular absorption database-2000 (HITRAN-2000) [*Rothman et al.*, 1992] with updates (aer_hitran_2000_updat_01.1). The input parameters include temperature and moisture profiles from the Global Forecast System (GFS) 12-h forecast, the SEVIRI LST retrieved from the GOES-R LSE algorithm, and the baseline fit LSE database [*Seemann*

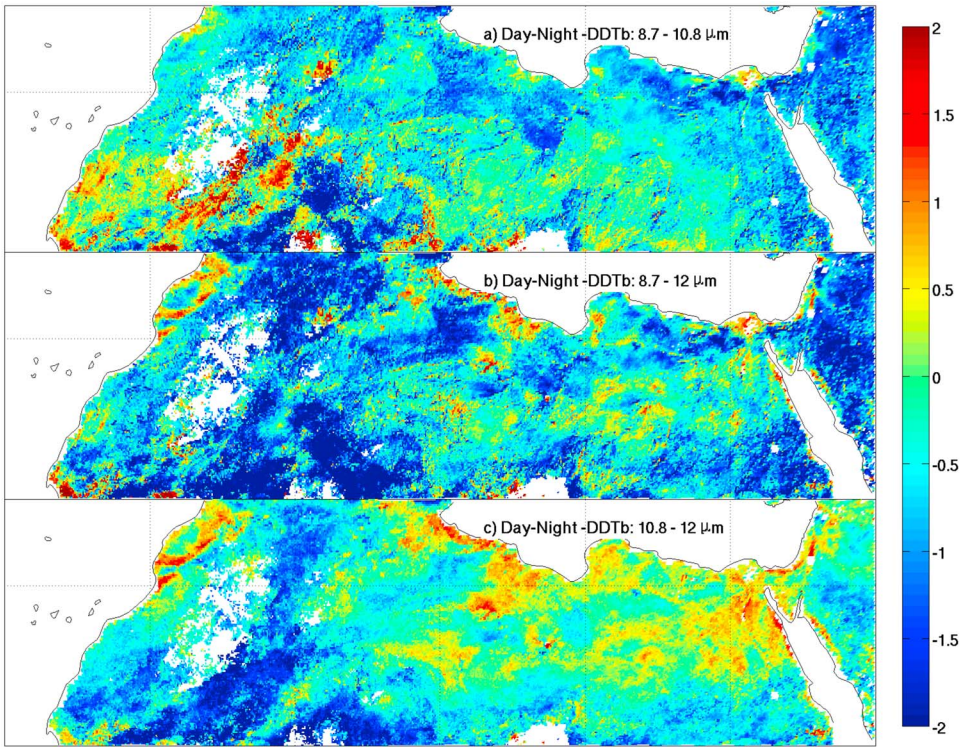


**Figure 8.** Day/night differences of SEVIRI -DDTb for August 2–7 2006 for (a) 8.7–10.8 $\mu$m, (b) 8.7–12 $\mu$m and (c) 10.8–12 $\mu$m.

*et al.*, 2008]. For the three window channels, the ozone profiles have limited impacts, and they are also retrieved from SEVIRI radiance observations using the GOES-R LSE algorithm. The cloud mask is processed using the GOES-R ABI cloud mask algorithm [*Heidinger et al.*, 2012].

[22] Figure 7 shows the day/night differences (day minus night) of LSE channel difference for the time period of August 2 to 7 of 2006. The day time is at 14 UTC and the nighttime is at 02 UTC, same as Figures 1–4. For all the three LSE channel differences, there are significant temporal variations (increasing) from 14 UTC to 02 UTC in most of the regions. 8.7–12 $\mu$m in the middle panel shows the strongest day/night differences among the three panels. This is because 12 $\mu$m has an opposite diurnal variation pattern as 8.7 $\mu$m. 10.8 and 8.7 $\mu$m LSE have similar diurnal variation patterns. As a result, 8.7–10.8 $\mu$m in the upper panel show smaller day/night differences. These results are consistent with those from August 1–31 of 2006 (not shown) except that the latter has less geographic gradients due to more samples to average. If the temporal variations of LSE channel differences shown in Figure 7 are real, the temporal variation of $-$ *DDTb* should have a similar geographic distribution providing there are no LST error diurnal variations (this will be shown in section 4.2).

[23] Figure 8 shows the day/night difference (day minus night) of $-$ *DDTb* for the time period of August 2 to 7 of 2006. The three panels in Figure 8 match with those in Figure 7 well geographically, but with noticeable differences. For most of the regions of significant negative values in Figure 7, Figure 8 show significant negative values accordingly. These are the regions of large LSE diurnal variations, possibly due to soil moisture change. There are also regions of large positive values of LSE diurnal variation, which can be seen in both Figures 7 and 8. Some of those regions can possibly be explained by cloud contamination. This is more noticeable to the south of 20°N (not shown in Figures 7 and 8), where it is closer to the ITCZ, and more prone to cloud contamination. In those regions, more extremely positive values are seen in all three panels. High similarity between Figure 7 and Figure 8 indicates that there are LSE diurnal variations in SEVIRI radiance observations; and there are no or very weak diurnal variations of SEVIRI LST error, which will be quantitatively shown in section 4.2.

### 4.2. Evidence From MODIS/Aqua Radiance Observations

[24] Section 4.1 shows that the diurnal variation of the retrieved SEVIRI LSE comes from the SEVIRI radiance observations, not artifacts from retrieval algorithm. It is still possible that SEVIRI radiance observations or the radiative transfer model PFAAST somehow have false diurnal bias, both of which result in false diurnal variation of retrieved LSE. The analysis presented in section 4.1 would not be able to identify that false diurnal information. Unless the same match could be seen using an independent source of measurements, the analysis in section 4.1 is not conclusive. In this section, MODIS/Aqua radiance observations are used to demonstrate the LSE diurnal variations. Aqua is chosen instead of Terra because of its local pass time is close to the chosen day time (14 UTC) and nighttime (02 UTC).

[25] It is noted that the three MODIS IR window channels (8.55, 11.03 and 12.02 $\mu$m) are slightly different from the

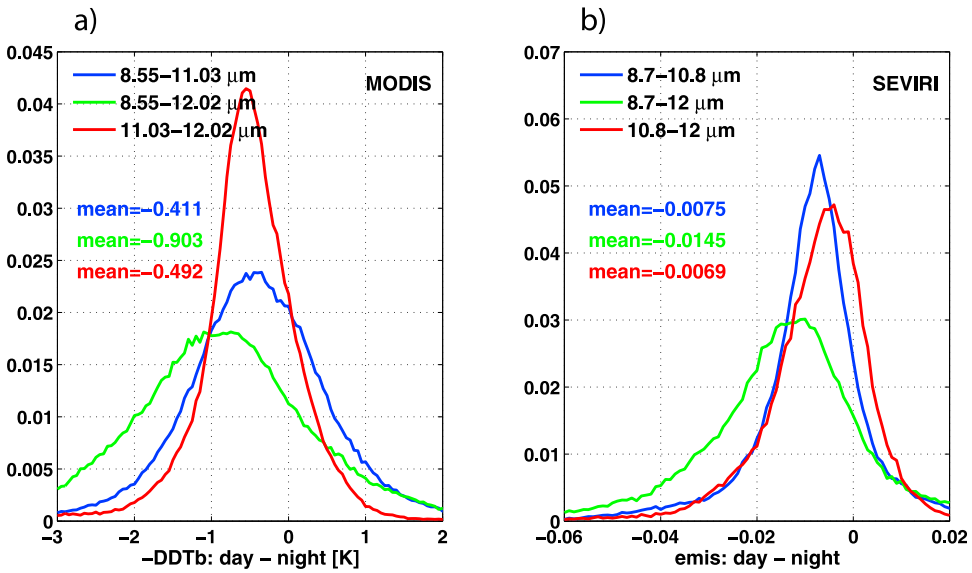


**Figure 9.** The normalized histograms of (a) the day/night differences of MODIS/Aqua –DDTb, and (b) the day/night differences of SEVIRI LSE channel differences for 2–7 August 2006.

SEVIRI (8.7, 10.8 and 12 $\mu$m). Since they are all broadband instruments and the spectra differences are very small, no spectra differences are considered in the process.

[26] To reduce the impacts from the radiative transfer model, the more sophisticated Community Radiative Transfer Model (CRTM) [*Chen et al.*, 2012] is used. The input parameters include temperature and moisture profiles from the Global Forecast System (GFS) 12-h forecast, the operational MODIS LST products (MYD11) version 4 (V4) [*Wan and Li*, 1997; *Wan*, 2008], and the baseline fit LSE database [*Seemann et al.*, 2008]. Again, ozone profiles are retrieved from the MODIS radiance observations using the GOES-R LSE algorithm. The MODIS cloud mask (MYD35) [*Ackerman*, 1997] is used to screen out cloudy pixels. It is found that the MODIS $-$ *DDTb* appears to have large negative bias when the local zenith angle is large. This angle dependency is more profound for polar orbiting satellites than geostationary satellites because the former has a wider range of local zenith angle over the Sahara Desert. To reduce the impacts from the angle, only pixels with local zenith angle smaller than 30 degree are retained. Instead of qualitative analysis presented in section 4.1, this section focuses on quantitative analysis to verify the consistency between SEVIRI and MODIS.

[27] Figure 9a shows the normalized histograms of the day/night differences of MODIS/Aqua $-$*DDTb*, and Figure 9b shows the normalized histograms of the day/night differences of SEVIRI LSE channel differences. The three MODIS/Aqua window channels are spectrally very close to the three SEVIRI channels. The temporal variations shown in Figure 9b could be considered the same as those from the MODIS/Aqua three window channels. Figures 9a and 9b look similar, but with substantial differences. The peaks of the three histograms in Figure 9a are all located to the left of zero line, same as those in Figure 9b. However, the peak of the red line of 11.03–12.02 $\mu$m is in the between of the peaks of the green line of 8.55–12.02 $\mu$m and the blue line of 8.55–11.03 $\mu$m in Figure 9a, while the blue line of 8.7–10.8 $\mu$m is in the middle in Figure 9b. The reason for the discrepancy is likely the MODIS/Aqua LST products (MYD11) have false diurnal variations, which will be quantitatively shown in the following. As a comparison, Figure 10a shows the normalized histogram of the day/night differences of SEVIRI $-$*DDTb*. The three histograms are located very similarly as shown in Figure 9b, indicating the LSE diurnal variations are the main cause of the SEVIRI $-$ *DDTb* diurnal variations.

[28] Figure 10b shows the sensitivity of MODIS/Aqua $-$ *DDTb* to the LST bias. When a 1 K LST bias is introduced, the three $-$ *DDTbs* have different sensitivities. 8.55–12.02 $\mu$m has the strongest sensitivity with a mean negative bias of $-0.137$ K, and 8.55–11.03 $\mu$m also has a mean negative bias of $-0.074$ K, while 11.03–12.02 $\mu$m has a mean positive bias of 0.0634 K. These values are actually the channel difference of the LST kernel functions in equation (6). With these sensitivity values, it is possible to calculate the day/night differences of LST error and verify the consistency between SEVIRI and MODIS/Aqua on identifying the LSE diurnal variations.

[29] In equation (6), the day/night differences of $-$ *DDTb* can be obtained using the mean values from the histogram of Figures 9a and 10a. The temporal variations of LSE channel differences can be obtained from Figure 9b. And the LST kernel function channel difference can be obtained from Figure 10b. Therefore, equation (6) can be written as

$$\begin{bmatrix} -0.465 & -0.411 \\ -0.887 & -0.903 \\ -0.423 & -0.492 \end{bmatrix} = \begin{bmatrix} -0.137 & -0.00753 \\ -0.074 & -0.0145 \\ 0.0634 & -0.00693 \end{bmatrix} \times \begin{bmatrix} \Delta\sigma_{T_s} \\ \delta\hat{\hat{K}}^{\varepsilon} \end{bmatrix}, \tag{7}$$

And the solutions are $\begin{bmatrix} \Delta\sigma_{T_s} \\ \delta\hat{\hat{K}}^{\varepsilon} \end{bmatrix} = \begin{bmatrix} 0.027 & -0.60 \\ 61.1 & 65.4 \end{bmatrix}$. These results indicate:

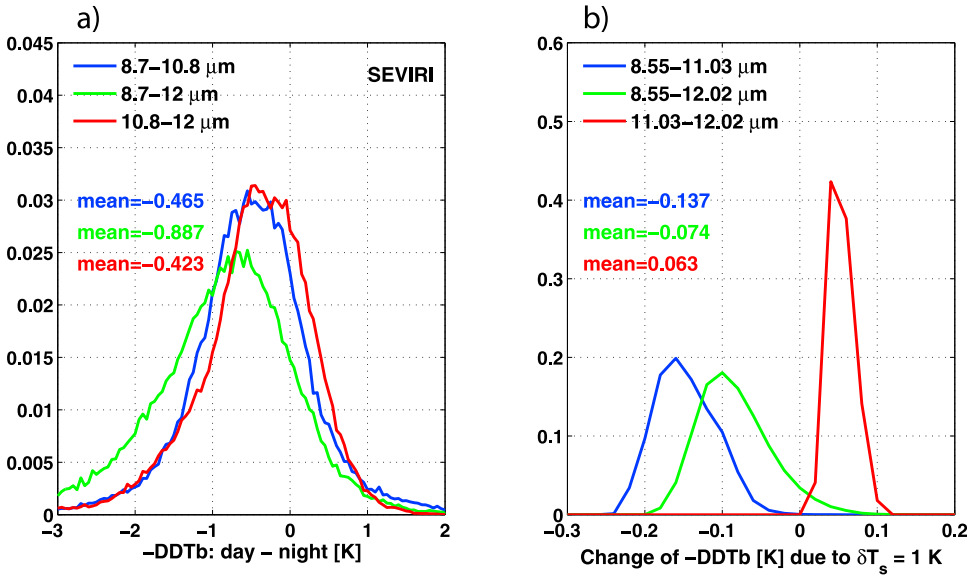


**Figure 10.** The normalized histograms of (a) the day/night differences of SEVIRI –DDTb for 2–7 August 2006, and (b) the change of MODIS/Aqua –DDTb due to a perturbation of LST change of 1 K.

[30] 1. There exists consistency between SEVIRI and MODIS/Aqua radiance observations on identifying LSE diurnal variations. The estimated mean LSE kernel functions are 61.1 and 65.4 K for SEVIRI and MODIS/Aqua, respectively. They are very close to each other, indicating both of them see LSE diurnal variations with a similar magnitude.

[31] 2. The actual LSE diurnal variations are likely larger than what is shown in this study. The estimated mean LSE weighing functions are larger than 60 K for both SEVIRI and MODIS/Aqua, larger than the normal value (around 50 K, estimated from radiative calculation). This indicates the temporal variations of LSE channel differences used in equation (7) (the values from Figure 9b) are likely smaller than they should be. The reason for that is because the retrieved LSE is a mean LSE of three time steps spanned in 6 h, which averages out the LSE diurnal variations.

[32] 3. MYD11 LST might have false diurnal variations. The estimated SEVIRI day/night difference of LST error is very close to zero, indicating the SEVIRI LST from GOES-R LSE algorithm captures the real LST diurnal variations well. There are no artificial SEVIRI LST diurnal variations on top of that. This does not mean there is no SEVIRI LST bias, but the SEVIRI LST bias does not diurnally change, if there is any. On the contrary, the MYD11 LST products have a day/night difference of LST error of −0.6 K, indicating there might exist artificial MYD11 LST diurnal variations. The possible reasons that MYD11 LST has artificial diurnal variations include 1) the MODIS day/night physical algorithm assumes that LSE does not change within 12 h or longer period of time [*Wan and Li*, 1997; *Wan*, 2008], and 2) errors in the atmospheric temperature/moisture profile [*Wan and Li*, 1997] retrieved from Aqua MODIS have false diurnal variations. This study shows that the LSE has wave-like diurnal variations with low values in the day and large values at night for SEVIRI 8.7 and 10.8 $\mu$m over the Sahara Desert. It is possible that the MODIS LSE has positive bias in the day and negative bias at night. In the retrieval, these LSE bias is converted to LST bias, negative in the day and positive at night. As a result, from day time to nighttime, the LST bias has a negative variation, as shown by the above solutions.

## 5. Discussion

[33] A major assumption of the technique presented in this study is the omission of atmospheric terms in equation (6), which is equivalent to saying that the GFS forecast temperature and moisture profile errors (bias) have no diurnal variations. This section discusses the impact of omission of diurnal variations of GFS forecast profile errors on the LSE retrieval.

[34] Figure 11 shows the mean bias of GFS forecast temperature and moisture profiles compared with ECMWF analysis in day time and nighttime for 2–7 August 2006. Only 500 hPa to the surface is presented because the three window channels are not sensitive to the upper troposphere in clear skies. From Figure 11, the GFS forecast underestimates the temperature near the surface at night (blue line), and overestimates it during the day (red line). The diurnal variations (day minus night; the black line) of the GFS forecast temperature error is substantial; the difference is more than 1.5 K around 940 hPa. Similarly, the GFS forecast moisture errors also have some substantial diurnal variations, when compared with those from the ECMWF analysis.

[35] In order to assess the impact of the diurnal variations of the GFS forecast error, a sensitivity study is performed by removing the GFS temperature and moisture bias (i.e., the GFS forecast profiles are adjusted so that both the day time and nighttime have no bias compared with ECMWF analysis), and these adjusted GFS forecast profiles are used in the GOES-R ABI LSE algorithm to derive the LSE. Figure 12 shows the mean LSE diurnal variations (day time minus nighttime) for 2–7 August 2006 before and after removing the diurnal variation of GFS forecast error. From Figure 12, the removal of GFS forecast profile bias reduces the diurnal variation of the retrieved SEVIRI LSE. And the reduction of

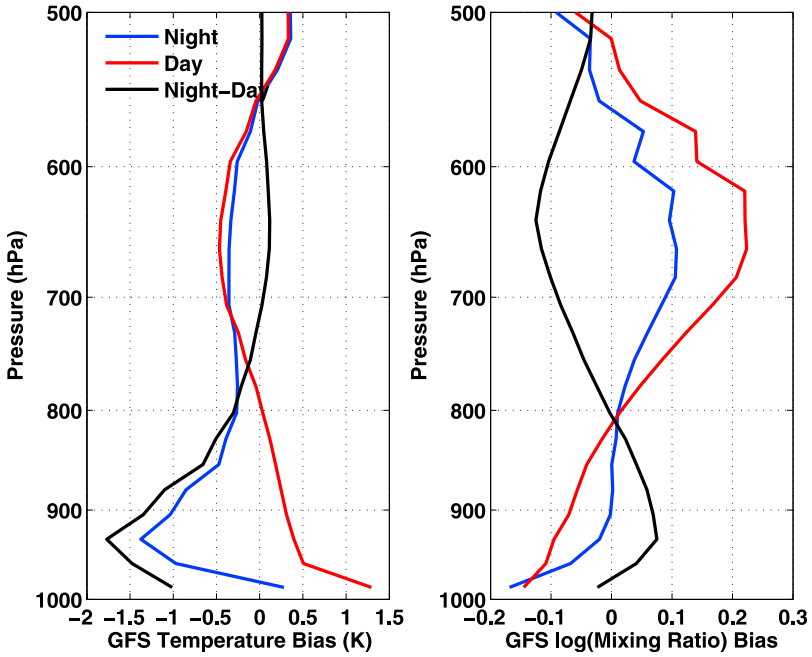


**Figure 11.** The mean bias of (left) the GFS forecast temperature and (right) the moisture (logarithm of mixing ratio) compared with ECMWF analysis for 2–7 August 2006. The blue lines represent nighttime (2 UTC), the blue lines represent-day time (14 UTC), and the black lines represent the diurnal variations (day minus night).

LSE diurnal variations is 12.0%, 15.4% and 16.6% for 8.7, 10.8 and 12.0 $\mu$m window channels respectively. This indicates the GFS forecast profile bias is a minor factor for the LSE diurnal variation presented in this study. In other words, the GFS forecast profile bias is unlikely the major contributor to the diurnal variations of the retrieved SEVIRI LSE.

## 6. Summary

[36] As part of GOES-R ABI LSE algorithm validation, the algorithm is applied to the SEVIRI radiance observations. The retrieved SEVIRI LSE show diurnal variations over the Sahara Desert from different time periods. The 8.7 $\mu$m band has the strongest wave-like diurnal variations with large values at night and small values in the day. The area and time averaged LSE day/night difference (day minus night) could be as large as $-0.0225$. The 10.8 $\mu$m has a similar diurnal variation pattern but with a weaker amplitude, about 1/3 of that of 8.7 $\mu$m in absolute value. The 12 $\mu$m has the weakest (about 1/6 of that of 8.7 $\mu$m in absolute value) diurnal variation among the three channels with an opposite phase. Further investigation is needed to explain why 12 $\mu$m has an opposite phase as the other two channels (10.8 and 8.7 $\mu$m). One possible reason is the aerosol contamination, which will have different radiative transfer impacts on the three IR window channels. No study has reported LSE diurnal variations, from either satellites or laboratory measurements. However, these results are consistent with previous studies regarding how LSE changes with soil moisture and how soil moisture diurnally varies.

[37] A method using satellite radiance observations is introduced to support that the LSE diurnal variations are real, not artifacts from the retrieval algorithm. The key of this method relies on the channel difference, which significantly minimizes the impacts from the atmosphere. Both SEVIRI and MODIS/Aqua radiance observations confirm the LSE diurnal variations over the Sahara Desert during the selected time. And both of them see a similar magnitude of the LSE diurnal variations. As a byproduct of the method, this study shows that the MODIS/Aqua LST products (MYD11) might have false diurnal variations; $-0.6$ K of

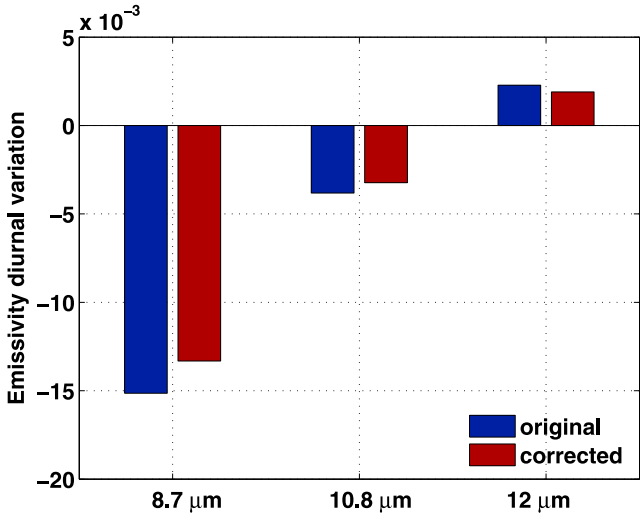


**Figure 12.** The mean SEVIRI LSE diurnal variations (day time minus nighttime) of the three window channels before and after the correction of GFS forecast profile bias for 2–7 August 2006.

day/night difference of LST error is estimated. The false MYD11 LST diurnal variations are likely due to the assumption of invariable LSE of day/night and the error in the atmospheric profiles. On the other hand, the SEVIRI LST products, generated by the GOES-R ABI algorithm, show no LST false diurnal variations because the LSE diurnal variations are captured well by the algorithm.

[38] The actual LSE diurnal variations are likely lager than what is shown in this paper, as supported by two facts. First, because the assumption of time continuity is used in the retrieval algorithm, the retrieved LSE is a mean LSE of three time steps over 6 hours. Due to the smoothing effect, the retrieved SEVIRI LSE is likely smaller than the real value at night and larger than the real value in the day, causing the SEVIRI LSE diurnal variations smaller than the actual value. This is also confirmed by the fact that the estimated mean LSE kernel functions (larger than 60 K) by both SEVIRI and MODIS/Aqua are larger than their mean values (around 50 K), which is a result of underestimated LSE diurnal variations.

[39] Experiments are conducted to investigate the impact of the GFS forecast profile errors (mean bias) on the diurnal variations of the retrieved SEVIRI LSE. It is found that the GFS forecast profiles have different biases between night and day as compared with the ECMWF analysis, and the removal of GFS forecast profile bias reduces the SEVIRI LSE diurnal variations. But the reduction is minor. It is concluded that the SEVIRI LSE diurnal variations demonstrated in this study are not likely due to the GFS forecast profile bias.

[40] This study focuses on LSE diurnal variations demonstration over Sahara Desert. There are at least two major factors affecting the LSE diurnal variations: the soil moisture content and the LSE sensitivity of the surface materials to the soil moisture. The soil moisture content varies geographically and temporally. It is possible that the LSE has smaller diurnal variations over some other types of land surface because LSE of those surface materials are less sensitive to soil moisture diurnal variations compared to sandy soil. However, most of the surface types other than desert likely have larger soil moisture content, and thus possibly stronger soil moisture diurnal variation. This essentially increases the possibility of LSE diurnal variations. Further investigation is needed to accurately estimate the uncertainty in LSE diurnal variation and to study how LSE diurnal variation is geographically and temporally dependent. This study has potential significance on both the retrieval community and the data assimilation community, potentially being able to exploit more satellite data over the land if the diurnal signature of LSE is taken into account.

[41] **Acknowledgments.** This work is partly supported by basic research program 2010CB950802, the National Oceanic and Atmospheric Administration (NOAA) GOES-R algorithm working group (AWG) and GOES-R Risk Reduction programs NA06NES4400002. The views, opinions, and findings contained in this report are those of the authors and should not be construed as an official National Oceanic and Atmospheric Administration or U.S. government position, policy, or decision. The authors would like to specifically thank Andrew K. Heidinger and William C. Straka for providing SEVIRI cloud mask products.

## References

Ackerman, S. A. (1997), Remote sensing aerosols using satellite infrared observations, *J. Geophys. Res.*, *102*(D14), 17,069–17,079, doi:10.1029/96JD03066.

Agam, N., and P. R. Berliner (2004), Diurnal water content changes in the bare soil of a coastal desert, *J. Hydrometeorol.*, *5*(5), 922–933, doi:10.1175/1525-7541(2004)005<0922:DWCCIT>2.0.CO;2.

Agam, N., and P. R. Berliner (2006), Dew formation and water vapor adsorption in semi-arid environments—A review, *J. Arid Environ.*, *65*(4), 572–590, doi:10.1016/j.jaridenv.2005.09.004

Becker, F., and Z. L. Li (1990), Toward a local split window method over land surface, *Int. J. Remote Sens.*, *11*, 369–393, doi:10.1080/01431169008955028.

Chahine, M. T., et al. (2006), AIRS: Improving weather forecasting and providing new data on greenhouse gases, *Bull. Am. Meteorol. Soc.*, *87*, 911–926, doi:10.1175/BAMS-87-7-911.

Chen, Y., Y. Han, and F. Weng (2012), Comparison of two transmittance algorithms in the community radiative transfer model: Application to AVHRR, *J. Geophys. Res.*, *117*, D06206, doi:10.1029/2011JD016656.

Clerbaux, C., J. Hadji-Lazaro, S. Turquety, G. Mégie, and P.-F. Coheur (2003), Trace gas measurements from infrared satellite for chemistry and climate applications, *Atmos. Chem. Phys. Discuss.*, *3*, 2027–2058, doi:10.5194/acpd-3-2027-2003.

Clough, S. A., and M. J. Iacono (1995), Line-by-line calculations of atmospheric fluxes and cooling rates: 2. Applications to carbon dioxide, ozone, methane, nitrous oxide and the halocarbons, *J. Geophys. Res.*, *100*, 16,519–16,535, doi:10.1029/95JD01386.

English, S. J., R. J. Renshaw, P. C. Dibben, A. J. Smith, P. J. Rayer, C. Poulsen, F. W. Saunders, and J. R. Eyre (2000), A comparison of the impact of TOVS and ATOVS satellite sounding data on the accuracy of numerical weather forecasts, *Q. J. R. Meteorol. Soc.*, *126*(569), 2911–2931.

Francois, C., C. Ottlé, and L. Prevot (1997), Analytical parameterization of canopy directional emissivity and directional radiance in the thermal infrared. Application on the retrieval of soil and foliage temperatures using two directional measurements, *Int. J. Remote Sens.*, *18*(12), 2587–2621, doi:10.1080/014311697217495.

Hannon, S., L. L. Strow, and W. W. McMillan (1996), Atmospheric infrared fast transmittance models: A comparison of two approaches, *Proc. SPIE*, *2830*, 94–105, doi:10.1117/12.256106.

Heidinger, A. K., A. T. Evan, M. J. Foster, and A. Walther (2012) A naive Bayesian cloud detection scheme derived from CALIPSO and applied to PATMOS-x, *J. App. Meteorol. Clim.*, *51*, 1129–1144, doi:10.1175/JAMC-D-11-02.1.

Hilton, F., et al. (2012), Hyperspectral Earth observation from IASI: Five years of accomplishments, *Bull. Am. Meteorol. Soc.*, *93*(3), 347–370, doi:10.1175/BAMS-D-11-00027.1.

Ho, S. P., D. P. Edwards, J. C. Gille, J. M. Chen, D. Ziskin, G. L. Francis, M. N. Deeter, and J. R. Drummond (2005), Estimates of 4.7 um surface emissivity and their impact on the retrieval of tropospheric carbon monoxide by Measurements of Pollution in the Troposphere (MOPITT), *J. Geophys. Res.*, *110*, D21308, doi:10.1029/2005JD005946.

Hulley, G. C., S. J. Hook, and A. M. Baldridge (2010), Investigating the effects of soil moisture on thermal infrared land surface temperature and emissivity using satellite retrievals and laboratory measurements, *Remote Sens. Environ.*, *114*, 1480–1493, doi:10.1016/j.rse.2010.02.002.

Jackson, T. J., P. E. O'Neill, and C. T. Swift (1997), Passive microwave observation of diurnal surface soil moisture, *IEEE Trans. Geosci. Remote Sens.*, *35*(5), 1210–1222, doi:10.1109/36.628788.

Jin, M., and S. Liang (2006), Improving land surface emissivity parameter of land surface models in GCM, *J. Clim.*, *19*, 2867–2881, doi:10.1175/JCLI3720.1.

Jin, X., J. Li, T. J. Schmit, J. Li, M. D. Goldberg, and J. J. Gurka (2008), Retrieving clear-sky atmospheric parameters from SEVIRI and ABI infrared radiances, *J. Geophys. Res.*, *113*, D15310, doi:10.1029/2008JD010040.

Kidron, G. J. (2000), Analysis of dew precipitation in three habitats within a small arid drainage basin, Negev Highlands, Israel, *Atmos. Res.*, *55*(3–4), 257–270, doi:10.1016/S0169-8095(00)00063-6.

Lee, H.-T., A. Gruber, R. G. Ellingson, and I. Laszlo (2007), Development of the HIRS outgoing longwave radiation climate data set, *J. Atmos. Oceanic Technol.*, *24*, 2029–2047, doi:10.1175/2007JTECHA989.1.

Le Marshall, J., et al. (2006), Improving global analysis and forecasting with AIRS, *Bull. Am. Meteorol. Soc.*, *87*, 891–894, doi:10.1175/BAMS-87-7-891.

Li, J. (1994), Temperature and water vapor weighting functions from radiative transfer equation with surface emissivity and solar reflectivity, *Adv. Atmos. Sci.*, *11*, 421–426, doi:10.1007/BF02658162.

Li, J., and H.-L. Huang (1999), Retrieval of atmospheric profiles from satellite sounder measurements by use of the discrepancy principle, *Appl. Opt.*, *38*(6), 916–923, doi:10.1364/AO.38.000916.

Li, J., and J. Li (2008), Derivation of global hyperspectral resolution surface emissivity spectra from advanced infrared sounder radiance measurements, *Geophys. Res. Lett.*, *35*, L15807, doi:10.1029/2008GL034559.

Li, J., W. Wolf, W. P. Menzel, W. Zhang, H.-L. Huang, and T. H. Achtor (2000), Global soundings of the atmosphere from ATOVS measurements: The algorithm and validation, *J. Appl. Meteorol.*, *39*, 1248–1268, doi:10.1175/1520-0450(2000)039<1248:GSOTAF>2.0.CO;2.

Li, J., W. P. Menzel, and A. J. Schreiner (2001), Variational retrieval of cloud parameters from GOES sounder longwave cloudy radiance measurements, *J. Appl. Meteorol.*, *40*, 312–330, doi:10.1175/1520-0450(2001)040<0312:VROCPF>2.0.CO;2.

Li, J., et al. (2005), Retrieval of cloud microphyiscal properties from MODIS and AIRS, *J. Appl. Meteorol.*, *44*, 1526–1543, doi:10.1175/JAM2281.1.

Li, J., P. Zhang, T. J. Schmit, J. Schmetz, and W. P. Menzel (2007a), Quantitative monitoring of a Saharan dust event with SEVIRI on Meteosat-8, *Int. J. Remote Sens.*, *28*, 2181–2186, doi:10.1080/01431160600975337.

Li, J., J. Li, E. Weisz, and D. K. Zhou (2007b), Physical retrieval of surface emissivity spectrum from hyperspectral infrared radiances, *Geophys. Res. Lett.*, *34*, L16812, doi:10.1029/2007GL030543.

Li, J., Z. Li, X. Jin, T. J. Schmit, L. Zhou, and M. Goldberg (2011), Land surface emissivity from high temporal resolution geostationary infrared imager radiances: 1. Methodology and simulation studies, *J. Geophys. Res.*, *116*, D01304, doi:10.1029/2010JD014637.

Li, Z., J. Li, W. P. Menzel, T. J. Schmit, J. P. Nelson III, J. Daniels, and S. A. Ackerman (2008), GOES sounding improvement and applications to severe storm nowcasting, *Geophys. Res. Lett.*, *35*, L03806, doi:10.1029/2007GL032797.

Li, Z., J. Li, W. P. Menzel, J. P. Nelson III, T. J. Schmit, E. Weisz, and S. A. Ackerman (2009), Forecasting and nowcasting improvement in cloudy regions with high temporal GOES sounder infrared radiance measurements, *J. Geophys. Res.*, *114*, D09216, doi:10.1029/2008JD010596.

Li, Z., J. Li, X. Jin, T. J. Schmit, E. Borbas, and M. Goldberg (2010), An objective methodology for infrared land surface emissivity evaluation, *J. Geophys. Res.*, *115*, D22308, doi:10.1029/2010JD014249.

Liu, C., J. Li, E. Weisz, T. J. Schmit, S. A. Ackerman, and H. L. Huang (2008), Synergistic use of AIRS and MODIS radiance measurements for atmospheric profiling, *Geophys. Res. Lett.*, *35*, L21802, doi:10.1029/2008GL035859.

Ma, X. L., T. J. Schmit, and W. L. Smith (1999), A non-linear physical retrieval algorithm—Its application to the GOES-8/9 sounder, *J. Appl. Meteorol.*, *38*, 501–513, doi:10.1175/1520-0450(1999)038<0501:ANPRAI>2.0.CO;2.

McAtee, B., A. F. Prata, and M.-J. Lynch (2003), The behavior of emitted thermal infrared radiation (8–12 $\mu$m) at a semiarid site, *J. Appl. Meteorol.*, *42*(8), 1060–1071, doi:10.1175/1520-0450(2003)042<1060:TABOET>2.0.CO;2.

McNally, A. P., P. D. Watts, J. A. Smith, R. Engelen, G. A. Kelly, J. N. Thepaut, and M. Matricardi (2006), The assimilation of AIRS radiance data at ECMWF, *Q. J. R. Meteorol. Soc.*, *132*(616), 935–957, doi:10.1256/qj.04.171.

Menzel, W. P., and J. F. W. Purdom (1994), Introducing GOES-I: The first of a new generation of Geostationary Operational Environmental Satellites, *Bull. Am. Meteorol. Soc.*, *75*, 757–781, doi:10.1175/1520-0477(1994)075<0757:IGITFO>2.0.CO;2.

Menzel, W. P., D. P. Wylie, and K. I. Strabala (1992), Seasonal and diurnal changes in cirrus clouds as seen in four years of observations with VAS, *J. Appl. Meteorol.*, *31*, 370–385, doi:10.1175/1520-0450(1992)031<0370:SADCIC>2.0.CO;2.

Menzel, W. P., F. C. Holt, T. J. Schmit, R. M. Aune, A. J. Schreiner, G. S. Wade, and D. G. Gray (1998), Application of GOES-8/9 soundings to weather forecasting and nowcasting, *Bull. Am. Meteorol. Soc.*, *79*, 2059–2077, doi:10.1175/1520-0477(1998)079<2059:AOGSTW>2.0.CO;2.

Menzel, W., R. Frey, H. Zhang, D. Wylie, C. Moeller, R. Holz, B. Maddux, B. Baum, K. Strabala, and L. Gumley (2008), MODIS global cloud-top pressure and amount estimation: Algorithm description and results, *J. Appl. Meteorol. Climatol.*, *47*(4), 1175–1198, doi:10.1175/2007JAMC1705.1.

Mira, M., E. Valor, R. Boluda, V. Caselles, and C. Coll (2007), Influence of soil water content on the thermal infrared emissivity of bare soils: Implication for land surface temperature determination, *J. Geophys. Res.*, *112*, F04003, doi:10.1029/2007JF000749.

Ogawa, K., and T. Schmugge (2004), Mapping surface broadband emissivity of the Sahara Desert using ASTER and MODIS data, *Earth Interact.*, *8*(7), 1–14, doi:10.1175/1087-3562(2004)008<0001:MSBEOT>2.0.CO;2.

Ogawa, K., T. Schmugge, and S. Rokugawa (2006), Observations of the dependence of the thermal infrared emissivity on soil moisture, *Geophys. Res. Abstr.*, *8*, 04996.

Peres, L. F., and C. C. DaCamara (2005), Emissivity maps to retrieve land-surface temperature from MSG/SEVIRI, *IEEE Trans. Geosci. Remote Sens.*, *43*(8), 1834–1844, doi:10.1109/TGRS.2005.851172.

Rothman, L. S., et al. (1992), The HITRAN molecular database: Editions of 1991 and 1992, *J. Quant. Spectrosc. Radiat. Transfer*, *48*, 469–507, doi:10.1016/0022-4073(92)90115-K.

Sanchez, J. M., A. N. French, and M. Mira (2011), Thermal infrared emissivity dependence on soil moisture in field conditions, *IEEE Trans. Geosci. Remote Sens.*, *49*(11), 4652–4659.

Schmetz, J., P. Pili, S. Tjemkes, D. Just, J. Kerkman, S. Rota, and A. Ratier (2002), An introduction to Meteosat Second Generation (MSG), *Bull. Am. Meteorol. Soc.*, *83*(7), 977–992, doi:10.1175/1520-0477(2002)083<0977:AITMSG>2.3.CO;2.

Schmit, T. J., and M. M. Gunshor, W. P. Menzel, J. J. Gurka, J. Li, and A. S. Bachmeier (2005), Introducing the next-generation advanced baseline imager on GOES-R, *Bull. Am. Meteorol. Soc.*, *86*(8), 1079–1096, doi:10.1175/BAMS-86-8-1079.

Seemann, S., E. Borbas, R. Knuteson, H.-L. Huang, G. R. Stephenson, and H.-L. Huang (2008), Development of a global infrared land surface emissivity database for application to clear sky sounding retrievals from multispectral satellite radiance measurements, *J. Appl. Meteorol.*, *47*, 108–123, doi:10.1175/2007JAMC1590.1.

Snyder, W. C., Z. Wan, Y. Zhang, and Y.-Z. Feng (1998), Classification-based emissivity for land surface temperature measurement from space, *Int. J. Remote Sens.*, *19*(14), 2753–2774, doi:10.1080/014311698214497.

Trigo, I. F., and P. Viterbo (2003), Clear sky window channel radiances: A comparison between observations and the ECMWF model, *J. Appl. Meteorol.*, *42*(10), 1463–1479, doi:10.1175/1520-0450(2003)042<1463:CWCRAC>2.0.CO;2.

Wan, Z. (2008), New refinements and validation of the MODIS land-surface temperature/emissivity products, *Remote Sens. Environ.*, *112*, 59–74.

Wan, Z., and J. Dozier (1996), A generalized split-window algorithm for retrieving land-surface temperature from space, *IEEE Trans. Geosci. Remote Sens.*, *34*, 892–905, doi:10.1109/36.508406.

Wan, Z., and Z.-L. Li (1997), A physics-based algorithm for retrieving land-surface emissivity and temperature from EOS/MODIS data, *IEEE Trans. Geosci. Remote Sens.*, *35*, 980–996, doi:10.1109/36.602541.

Yu, Y., J. L. Privette, and A. C. Pinheoro (2008), Evaluation of split window land surface temperature algorithms for generating climate data records, *IEEE Trans. Geosci. Remote Sens.*, *46*, 179–192, doi:10.1109/TGRS.2007.909097.

Zhang, P., N. Lu, X. Hu, and C. H. Dong (2006), Identification and physical retrieval of dust storm using three MODIS thermal IR, *Global Planet. Change*, *52*, 197–206, doi:10.1016/j.gloplacha.2006.02.014.

Zhou, L., M. Goldberg, C. Barnet, Z. Cheng, F. Sun, W. Wolf, T. King, X. Liu, H. Sun, and M. Divakarla (2008), Regression of surface spectral emissivity from hyperspectral instruments, *IEEE Trans. Geosci. Remote Sens.*, *46*, 328–333, doi:10.1109/TGRS.2007.912712.